Available online at www.sciencedirect.com
ScienceDirect
Journal of Nuclear Materials 375 (2008) 173–184
journal of nuclear materials
www.elsevier.com/locate/jnucmat

High temperature reactivity of two chromium-containing alloys in impure helium

C. Cabet [a,*], J. Chapovaloff [b], F. Rouillard [a], G. Girardin [b], D. Kaczorowski [c], K. Wolski [d], M. Pijolat [e]

[a] Laboratoire d'Etude de la Corrosion Non Aqueuse, DEN/DANS/DPC/SCCME, CEA Saclay, F-91191 Gif-sur-Yvette, France
[b] Corrosion-Chemistry Department, Technical Center, AREVA NP, 1 rue B. Marcet, BP 181, F-71205 Le Creusot, France
[c] FDEEM – Metallic Alloy Group, Fuel Sector, AREVA NP, 10 rue Juliette Récamier, F-69456 Lyon cedex 06, France
[d] Centre SMS/MPI, UMR-CNRS 5146, Ecole Nationale Supérieure des Mines, 158 cours Fauriel, F-42023 Saint Etienne, France
[e] Département ProcESS, LPMG CNRS URA 2021, Centre SPIN, Ecole Nationale Supérieure des Mines, 158 cours Fauriel, F-42023 Saint Etienne, France

Received 22 February 2007; accepted 13 November 2007

Abstract

Chromium-rich nickel base alloys 617 and 230 are promising candidate materials for very high temperature gas-cooled reactors (VHTR) but they must resist corrosion in the impure primary cooling helium over very long times. The impurities of the hot helium can promote the development of chromium-rich surface oxides that appear to protect the alloys against intensive corrosion processes. However above a critical temperature (typically in the range 1173–1273 K), chromium oxide is reduced by carbon from the alloy and the surface layer is not stable anymore. Depending on the gas composition, the unprotected material rapidly either gains or loses carbon with a dramatic impact on its mechanical properties. The deleterious reaction of chromia and carbon thus fixes an ultimate reactor operating temperature. Critical temperature measurements are presented for alloys 617 and 230 and the influence of carbon monoxide partial pressure in helium is discussed.

PACS: 81.05.Bx; 81.65.Mq; 82.65.−r

1. Introduction

The ANTARES program [1] of AREVA NP aims at developing a very high temperature gas-cooled reactor (VHTR) to produce electricity and hydrogen or to supply any other industrial plant requiring high temperature process heat. The concept is based on a modular gas-cooled reactor (GCR) operating at high temperature (maximum 1123–1223 K) in indirect cycle. The thermal power produced in the reactor core is transferred from the primary coolant, namely helium, to a secondary circuit via a heat exchanger, the intermediate heat exchanger (IHX). Compact systems, such as plate-fin or plate machined heat exchangers, could be the most competitive lay-outs with only one IHX vessel component. However these concepts are highly demanding toward structural materials because very thin metallic sheets must be mechanically resistant and leak-tight at temperatures as high as 1223 K (for a specific ANTARES variant). Moreover, the IHX shall be designed for an extensive life time of typically 20 years.

A joint R&D program is currently underway in France between CEA, AREVA NP and EDF to select and qualify IHX candidate alloys. The selection is based on the structural stability, the creep strength and the compatibility with the coolant. This paper focuses on the compatibility of alloys with the primary helium coolant. This subject has already been investigated in the 70s and 80s and is said

* Corresponding author. Tel.: +33 169 08 16 15; fax: +33 169 08 15 86.
E-mail address: celine.cabet@cea.fr (C. Cabet).

0022-3115/$ - see front matter © 2008 Elsevier B.V. All rights reserved.
doi:10.1016/j.jnucmat.2007.11.006

to be essentially problematic at the highest temperatures at which some alloys may suffer from major corrosion damages.

Most of the past experience relates to nickel base alloys, rich in chromium for the oxidation resistance, and strengthened by additions of molybdenum and cobalt (especially Alloy 617 and Alloy X). In the last decades, tungsten tended to replace molybdenum as an additive element for the reinforcement of nickel base alloys at elevated temperatures. Based on its promising creep properties, Alloy 230 (14 wt% W) could be a candidate material for IHX applications but its corrosion resistance has never been investigated in the VHTR environment.

In the framework of their corrosion programs, CEA and AREVA NP study the surface reactivity, respectively of Alloy 230 and of Alloy 617 in the range 723–1253 K under impure helium representative of the VHTR primary coolant. Part of these investigations has already been published [2–5]. In this paper, we compare the results from the two teams and discuss them regarding the influence of the gas composition and the effect of the alloy chemistry.

2. Literature survey on the high temperature corrosion of Ni–Cr–Mo alloys in impure helium

2.1. Characteristics of the VHTR helium

Despite a highly gastight design and efficient purification systems, the VHTR primary coolant will inevitably contain residual contaminants coming from the outgassing of adsorbed species out of the permanent components (reflectors, insulation) and the fuel elements, and from air-ingresses during maintenance and refueling, and from in-leakages [6]. Experience from the former helium-cooled reactors allows the estimation of the pollution level. Table 1 gives the available data on the coolant analysis in three experimental reactors [8,9]. Impurities are water vapor and permanent gases such as H_2, CO, CO_2, CH_4, N_2... It was observed that the contamination was high at start-up [7], and then progressively decreased to a very low steady state level [6] as a dynamic balance established between the pollution rates, the reactions of the pollutants with hot graphite and metallic materials, and the purification efficiency. We expect that the technological evolutions from past reactors to advanced VHTRs shall change the impurity contents in the following ways:

- the improved tightness shall decrease the overall leak rate,
- the ANTARES design (secondary circuit, electricity production via a gas turbine) eliminates the contamination (H_2O, H_2) from the steam generators,
- the use of up-to-date lubricant-free bearings suppresses oil or water in-leakages,
- operations at higher temperature promote CO vs. CO_2 and destabilize CH_4 vs. H_2 [7].

Table 1
Impurity contents (in Pa) in experimental helium-cooled reactors – H_2, H_2O, CO_2, CO, CH_4 after Ref. [9] and N_2 after Ref. [8]

	H_2	H_2O	CO_2	CO	CH_4	N_2
DRAGON	2	0.1	0.04	1	0.3	1.2
AVR	30	3	10	30	–	
Peach bottom	20	<1	–	1	1.5	1.5

Finally, it is expected that the VHTR helium should contain H_2, CO (and CO_2), CH_4, N_2 ranging from one Pa or so to some tens of Pa and water vapor in the tenth of Pa range. It is worth noticing that extremely low free oxygen concentrations are expected because of the fast reaction between molecular oxygen and hot graphite.

2.2. Gas/metal surface reactions in impure helium

Because of the low impurity contents and of the very high flow velocity of helium in the reactor core, the collision probability between gaseous molecules is very low and the gas phase does not achieve equilibrium [8]. The impure helium can therefore not be ascribed through a mere thermodynamic approach. It is assumed that the gas/surface reactions can be regarded as independent [10,11]. Besides, nitrogen was demonstrated to be fairly inert in the given conditions – very low concentrations – and does not significantly contribute to the corrosion [12]. Therefore the set of possible equations between one helium impurity and the metallic surface is illustrated below [10–13]:

- Oxidation of the metal by the *water vapor*
$$x\mathrm{H_2O_{(g)}} + \mathrm{Me_{(s)}} = \mathrm{MeO}_{x(s)} + x/2\mathrm{H_{2(g)}} \quad (1)$$
- Decomposition of the *methane* on the metallic surface
$$\mathrm{CH_{4(g)}} = \mathrm{C_{(s)}} + 2\mathrm{H_{2(g)}} \quad (2)$$
- Reaction of the *water vapor* with carbon from the alloy
$$\mathrm{H_2O_{(g)}} + \mathrm{C_{(s)}} \rightarrow \mathrm{CO_{(g)}} + \mathrm{H_{2(g)}} \quad (3)$$
- Decomposition of the *carbon monoxide* with metal oxidation
$$x\mathrm{CO_{(g)}} + \mathrm{Me_{(s)}} \rightarrow \mathrm{MeO}_{x(s)} + x\mathrm{C_{(s)}} \quad (4)$$

$Me_{(s)}$ is a metal of the alloy that can be oxidized at the low oxygen potential prevailing in the VHTR helium such as Al, Si, Ti, Mn, Cr... (Fe, Co, Ni... are too inert to react in the given conditions) and MeO_x is the corresponding oxide. The former studies on Ni–Cr–Mo alloys highlighted the key role of chromium in the metallic carbides as well as in the surface oxide.

Eqs. (1)–(4) use the carbon in solution $C_{(s)}$ but a similar set of equations may also be written with the internal carbides Me_xC_y, or more specifically Cr_3C_2 or $Cr_{23}C_6$, assuming that carbides and $C_{(s)}$ are in equilibrium within the substrate, according to

$$\mathrm{Cr_{23}C_{6(s)}} = 6\mathrm{C_{(s)}} + 23\mathrm{Cr_{(s)}} \quad (5)$$

2.3. Corrosion effects

Generally speaking, the high temperature resistance of Ni–Cr–Mo alloys relies on the formation of a chromium-rich surface oxide scale that must be adherent, dense, and slow-growing – one says 'protective'. This layer actually protects the metal against corrosive gasses. For its long term resistance, the IHX material must thus definitely oxidize in the VHTR environment. Accordingly Eq. (1) must occur and overcome all Eqs. (2)–(4) which implies the following conditions [10,11,13,14]:

- The $P(H_2O)/P(H_2)$ ratio, related to the oxygen potential, must be oxidizing in respect to chromium,
- It is necessary to balance the content of carbon-bearing gasses such as methane (and potentially carbon monoxide [10,11]) relatively to the water vapor concentration.

A porous (or even no) surface layer form, if Eqs. (2) and (3) and/or Eq. (4) takes place, possibly coupled to Eq. (1). So, the impure helium exchanges carbon with the metal. This carbon transfer not only modifies the surface corrosion products (oxides and/or carbides), but also causes in-depth changes in the alloy microstructure, detrimental to the mechanical properties:

- *Carburization:* A carbon deposit on the surface can diffuse deeper into the bulk. If the carbon concentration locally reaches the solubility limit, coarse internal carbides precipitate that embrittle Ni–Cr–Mo alloys at low temperature [15]. Moreover, carburization strongly lowers the creep strain [16,17] even if it is said to have few effects on the creep rupture life [18].
- *Decarburization:* Carbon removal from the surface causes a transport of carbon to the surface. The decrease in the carbon content triggers the dissolution of the internal carbides that can lower the creep properties of carbide-strengthened alloys [19].

2.4. Oxide scale reduction

Besides Eqs. (1)–(4) a further specific process, named 'microclimate reaction' by Brenner [10,11], takes place at the highest temperatures, typically around 900–950 °C. Eq. (6) is formally the back equation of Eq. (4)

$$MeO_{x(s)} + xC_{(s)} \overset{T>T_A}{\rightarrow} xCO_{(g)} + Me_{(s)} \quad (6)$$

From the experimental point of view, it is as if Eq. (4) reverses at a critical temperature T_A for given surface activities of $C_{(s)}$ and $Me_{(s)}$, and a given partial pressure of carbon monoxide in helium [12].

At temperatures above T_A, the surface MeO_x can no longer co-exist with the carbon from the alloy and Eq. (6) proceeds until either all the oxide or all the carbon is removed, if the parameters remain constant. Brenner [10,11] emphasized the major influence of the $P(CH_4)/P(H_2O)$ ratio. At a low $P(CH_4)/P(H_2O)$ ratio, the metal produced by Eq. (6) reacts with water vapor according to Eq. (1) regenerating the oxide while the alloy in-depth decarburizes. Due to the production of gaseous carbon monoxide the surface layer is porous and does not provide any protection anymore. At a high $P(CH_4)/P(H_2O)$ ratio, the metal produced by Eq. (6) reacts with methane according to Eq. (2) leading to an extensive carburization of the substrate.

Whatever the direction of the carbon transfer, carburization or decarburization, above T_A, the corrosion goes in an active way that alters the mechanical properties (see Section 2.3). Because of Eq. (6), VHTR environment must fulfill a further criterion in order to secure a long lifetime of the IHX material: for a given $P(CO)$ in the helium coolant, the temperature must stay below T_A (in other words at a given service temperature, $P(CO)$ in the gas phase must be higher than a critical value).

It is worth noticing that the exact scheme of Eq. (6) is under debate since some authors [10,11,14,20,21] consider that solid/solid reactions are unlikely for kinetic reasons. Gaseous intermediates might take part in the reaction scheme. H_2/H_2O or CO/CO_2 could act as catalysts in a small diffusion-controlled gas layer near the two solids, oxide and alloy (that supplies $C_{(s)}$) [10–12,22].

2.5. Experimental determination of T_A

Quadakkers [20] developed a procedure to determine T_A for Alloy 617. First, a specimen is heated in the PNP standard atmosphere (see Table 2) up to 1123 K and the conditions are kept constant for 20 h so that the surface is passivated by oxidation due to Eq. (1), and possibly Eq. (4). The specimen is further heated up to 1223 K for 20 more hours. During heating from 1123 K to 1223 K, analyzers do not initially detect any change in the gas phase composition. But afterward, a dramatic increase in the partial pressure of carbon monoxide is observed. Then the carbon monoxide content slowly decreases when the temperature is kept constant at 1223 K. The production of the carbon monoxide begins at T_A, about1193 K in the present case. By repeating the experiment in helium with different carbon monoxide contents, Quadakkers [20] obtained a curve: T_A vs. $P(CO)$.

3. Experimental procedure

Within the framework of a joint R&D plan, AREVA NP, the CEA, and EDF have launched parallel experimental programs on the characterization of the IHX candidate materials in the VHTR operating conditions. Regarding the surface reactivity in impure helium, AREVA NP mainly investigates the high temperature behavior of Alloy 617 and the CEA works on Alloy 230. Each laboratory has built its own experimental loops and specific test procedures were developed. It is noteworthy that a benchmark experiment has been performed between the different labs

Table 2
Composition of the test helium mixtures and measured critical temperatures T_A; Alloy 617 was tested in He–In1 to He–In6 and Alloy 230 was tested in He–H1 to He–H5

	H_2 (Pa)	H_2O (Pa)	CO (Pa)	CH_4 (Pa)	T_A (K)
PNP [20]	50	0.15	1.5	2	1193
He–In1	16.00 ± 0.01	0.30 ± 0.10	0.18 ± 0.01		1156.0 ± 3.5
He–In2	50.00 ± 0.01	0.58 ± 0.10	1.39 ± 0.01		1193.0 ± 3.5
He–In3	50.00 ± 0.01	0.58 ± 0.10	1.46 ± 0.01		1194.0 ± 3.5
He–In4	12.80 ± 0.01	0.59 ± 0.10	1.42 ± 0.01		1194.0 ± 3.5
He–In5	50.00 ± 0.01	0.53 ± 0.10	2.63 ± 0.01		1220.0 ± 3.5
He–In6	2.70 ± 0.01	0.60 ± 0.10	5.80 ± 0.01		1245.0 ± 3.5
He–H1	20.0 ± 0.4	0.55 ± 0.24	0.60 ± 0.01	1.80 ± 0.04	1168 ± 5
He–H2	19.6 ± 0.4	0.03 ± 0.02	2.20 ± 0.04	1.89 ± 0.04	1213 ± 5
He–H3	19.3 ± 0.4	0.16 ± 0.08	4.90 ± 0.10	1.90 ± 0.04	1234 ± 5
He–H4	19.5 ± 0.4	0.17 ± 0.08	5.00 ± 0.10	2.02 ± 0.04	1237 ± 5
He–H5	19.6 ± 0.4	0.04 ± 0.02	5.30 ± 0.10	2.10 ± 0.04	1242 ± 5

Table 3
Chemical composition of Alloys 617 and 230 (in wt%) after the manufacturer certificates

	Ni	Cr	W	Co	Mo	Fe	Al	Mn	Ti	Si	Cu	C	B
Alloy 617	base	21.6	–	12.0	9.2	1.0	1.0	0.1	0.4	0.2	0.1	0.06	0.002
Alloy 230	base	22.0	14.7	0.2	1.3	1.3	0.4	0.5	0.1	0.4	–	0.105	0.002

in order to inter-validate the loops and the test procedures [23].

3.1. Materials

Inconel® alloy 617 was supplied by Special Metals Corporation as a cold rolled, solution annealed, 2 mm-thick sheet (heat treatment: 5 min at 1448 K, air cooling). Haynes® alloy 230 was produced by Haynes International, Inc. in the mill-annealed condition (annealing 10 min at 1503 K, water quenching). Table 3 reports the chemical composition of the alloys according to the analysis certificates by the manufacturers. Rectangular specimens (thickness: about 2 mm; area: 4.5 or 6 cm^2) were machined from the as-received materials. The specimen surface was ground to 2400 grit, finished with a 3 μm diamond paste or a 1 μm alumina powder, and then ultrasonically cleaned in acetone and ethanol.

3.2. Test loops

Two loops were used for the corrosion testing, one at AREVA NP and the other at the CEA. In both loops, the specimens are exposed to flowing impure helium at high temperature and atmospheric pressure. The impurity concentrations are analyzed at the test section inlet and outlet by gas phase chromatography (GPC). The residual moisture in helium is also monitored by a hygrometer.

The gas flow rates are approx. 0.7 and 2.4 ml/s per cm^2 of metallic surface, respectively in the loop of the CEA and in the loop of Areva NP. Blank tests were carried out without any specimen in the loops in order to check that the test section and specimen holder materials do not significantly react with gaseous impurities, or influence the gas composition.

3.3. Test conditions

Table 2 gives the impurity concentrations and the water vapor partial pressure in experimental helium mixtures. In any case, oxygen, nitrogen and carbon dioxide partial pressures were below the GPC detection limit (about 0.01 Pa). Alloy 617 was tested in He–In1 to He–In6 atmospheres and Alloy 230 in He–H1 to He–H5. The first tests on Alloy 617 at AREVA NP were carried out using the very same experimental procedure as Quadakkers [20] (see Section 2.5). This early protocol was later on adapted in order to increase the production of CO and so the accuracy on the determination of T_A. The improved test procedures consisted of two thermal steps and were specific to each lab:

- AREVA NP – Alloy 617 (see Fig. 1)

step 1: heating to 1123 K at 1.7 K/min and keeping the temperature constant for 20 h under impure helium,
step 2: heating to 1253 K at 0.5 K/min and keeping the temperature constant for 20 h under impure helium,
cooling: rapid cooling at about 3 K/min under impure helium.

- The CEA – Alloy 230 (see Fig. 5)

step 1: heating to 1173 K at 1 K/min and keeping the temperature constant for 25 h under impure helium,
step 2: heating to 1253 K at 0.5 K/min and keeping the temperature constant for 20 h under impure helium,
cooling: natural cooling under pure helium.

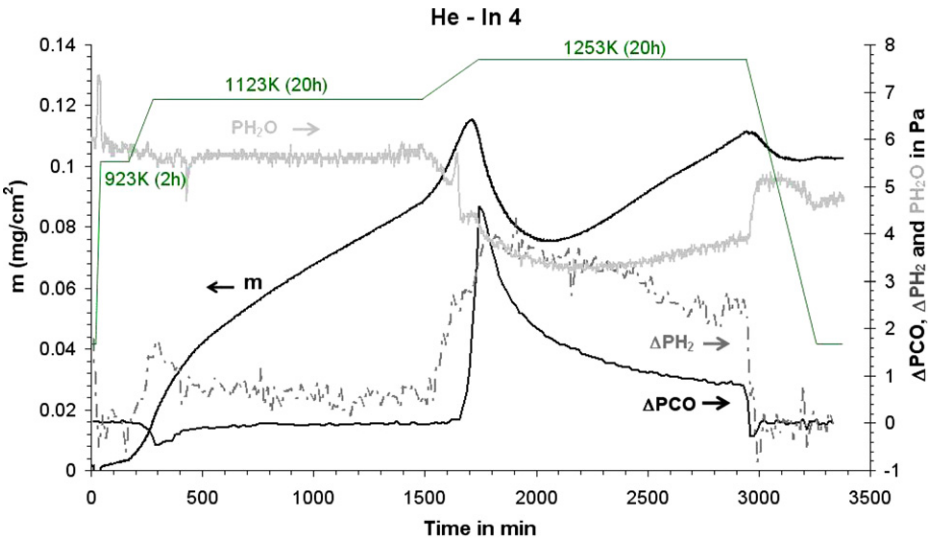

Fig. 1. Temperature program, outlet partial pressure of water vapor, and differences in the partial pressures of CO and of H_2 between outlet and inlet as a function of time – reactivity of Alloy 617 in He–In4.

3.4. Techniques of observation and analysis

After completion of the corrosion tests, the specimens were weighed. Some Alloy 230 specimens were analyzed without any specific preparation by X-ray diffraction (XRD with Cu Kα radiation) and by glow discharge optical emission spectroscopy (GDOES). The GDOES was systematically calibrated using metallic standards for a quantitative analysis of the carbon in the alloy. Cross-section coupons were sawed and prepared for observation. The mounted Alloy 617 coupons were ground to 2400 grit, finished with a 3 μm diamond paste and etched in chloroacetic acid. The Alloy 230 coupons were sputtered with a gold film using cathodic evaporation and then coated by an electrolytic nickel deposit (both layers are visible on micrographs) in order to improve the SEM image contrast and resolution as well as to prevent the oxide layer from spalling. After mounting, the Alloy 230 coupons were ground to 2400 grit and finished with a 1 μm alumina powder. Material surface was then characterized using field emission scanning electron microscopy (FESEM) and energy-dispersive X-ray spectroscopy (EDX).

4. Results

4.1. Determination of T_A and surface characterization of Alloy 617

As it was explained in Sections 2.4 and 2.5, it was observed [10,11,13,14,20,21] that above a critical temperature T_A and for a given partial pressure of carbon monoxide in helium, the surface oxide on Alloy 617 reacts according to Eq. (6) leading to a production of carbon monoxide. The purpose of the following experiments is to reproduce the former observations by Quadakkers [20] and to verify the proposed relation between T_A and $P(CO)$.

4.1.1. T_A measurements

The experimental method was derived from Ref. [20]. As it was already observed by Quadakkers, Fig. 1 shows that the carbon monoxide was initially consumed during the early stage of step 1 in helium He–In4. Then the partial pressure of carbon monoxide significantly increased at the test section outlet during step 2. Starting at about 1193 K, the carbon monoxide production reached 0.46 Pa, then it smoothly decreased and finally stabilized at about 0.08 Pa when the temperature was kept constant at 1253 K.

4.1.2. Observation and analysis of the Alloy 617 surface after step 1 (below T_A)

The thermobalance recorded a mass gain of 0.09 ± 0.01 mg/cm^2 for Alloy 617 after step 1 in He–In3. Fig. 2 shows the surface of a specimen of Alloy 617 exposed for 20 h at 1123 K in He–In3. The oxide scale consists of chromium oxide nodules over a continuous chromium oxide layer that contains some aluminum. Moreover titanium is analyzed above the alloy grain boundaries. Under the alloy surface, internal aluminum-rich oxides have formed at grain boundaries. Chromium- and molybdenum-rich carbides are also observed in the alloy bulk.

4.1.3. Observation and analysis of the Alloy 617 surface during step 2 (above T_A)

Fig. 3 shows the surface of a specimen of Alloy 617 exposed for 5 h at 1253 K in He–In3. This duration corresponds to the minimum in the mass of the specimen with $\Delta m = +0.04 \pm 0.01$ mg/cm^2. When compared to Fig. 2,

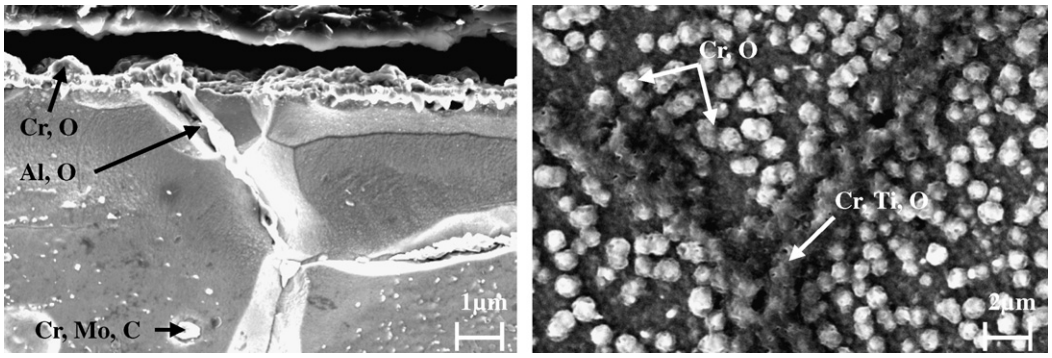

Fig. 2. FESEM images with a secondary electron contrast – cross section and top view of the Alloy 617 surface after step 1 in He–In3.

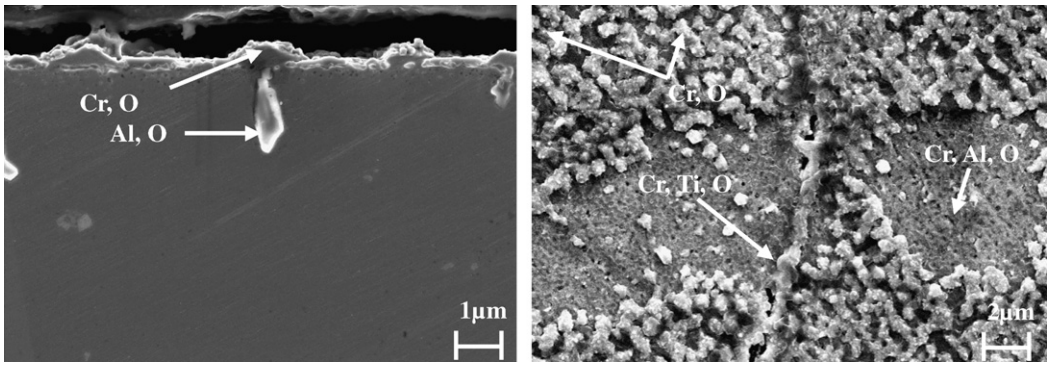

Fig. 3. FESEM images with a secondary electron contrast – cross section and top view of the Alloy 617 surface during step 2, after 5 h at 1253 K in He–In3.

the surface morphology is characterized by a significant reduction of the nodules.

4.1.4. Observation and analysis of the Alloy 617 surface after step 2 (above T_A)

For Alloy 617 in He–In3, the thermobalance recorded a higher mass gain ($\Delta m = +0.10 \pm 0.01$ mg/cm^2) after step 2 than after step 1. Fig. 4 shows the surface of a specimen of Alloy 617 after 20 h at 1253 K in He–In3. The surface scale seems more crystallized than in Fig. 2. It still consists of a chromium-rich oxide but its aluminum content is higher than after step 1. Titanium is preferentially detected above the alloy grain boundaries. In the near-surface region, aluminum is detected as an internal oxide. It is noteworthy that no carbide is observed under the surface up to about 120 μm deep.

4.2. Reactivity of Alloy 230

The following experiments aim at characterizing the high temperature reactivity of Alloy 230, in particular its susceptibility to Eq. (6).

4.2.1. Gas phase analyses

Fig. 5 presents the gas phase analysis by GPC during testing of Alloy 230 in helium He–H3. As observed for Alloy 617, during step 1 (heating to 1173 K and stay for 25 h) the P(CO) curve exhibits a negative peak that can be attributed to Eq. (4) [2]. During step 2 (heating to 1253 K and stay for 20 h) the partial pressure of carbon monoxide increased. Starting roughly at 1243 ± 5 K, the CO production reached 0.9 Pa. Afterward, the partial pressure of carbon monoxide slowly decreased to a level of about 0.3 Pa when the temperature was kept constant at 1253 K.

4.2.2. Mass changes

Table 4 reports the mass change of the Alloy 230 specimens after step 1 and after step 2 under impure helium He–H3. After both steps, the specimen mass increased but the average mass gain after step 2 was twice less than after step 1. As the specimens did not spall, the difference in the gains can definitely be related to a mass loss during step 2.

4.2.3. Observations and analyses of the Alloy 230 surface after step 1 (below T_A)

Fig. 6, left-hand side, shows the surface of a specimen of Alloy 230 exposed for 25 h at 1173 K in He–H3. Table 4 gives the approximate mean scale thickness after step 1 as estimated by microscopy. A continuous scale, about 0.7 μm thick, has formed on the surface. Grazing XRD analysis at 1° identified Cr_2O_3 and the spinel phase $Mn_{1.5}Cr_{1.5}O_4$ type (see Fig. 7). A wavelength dispersive X-ray spectrometry (WDS) linescan through the layer

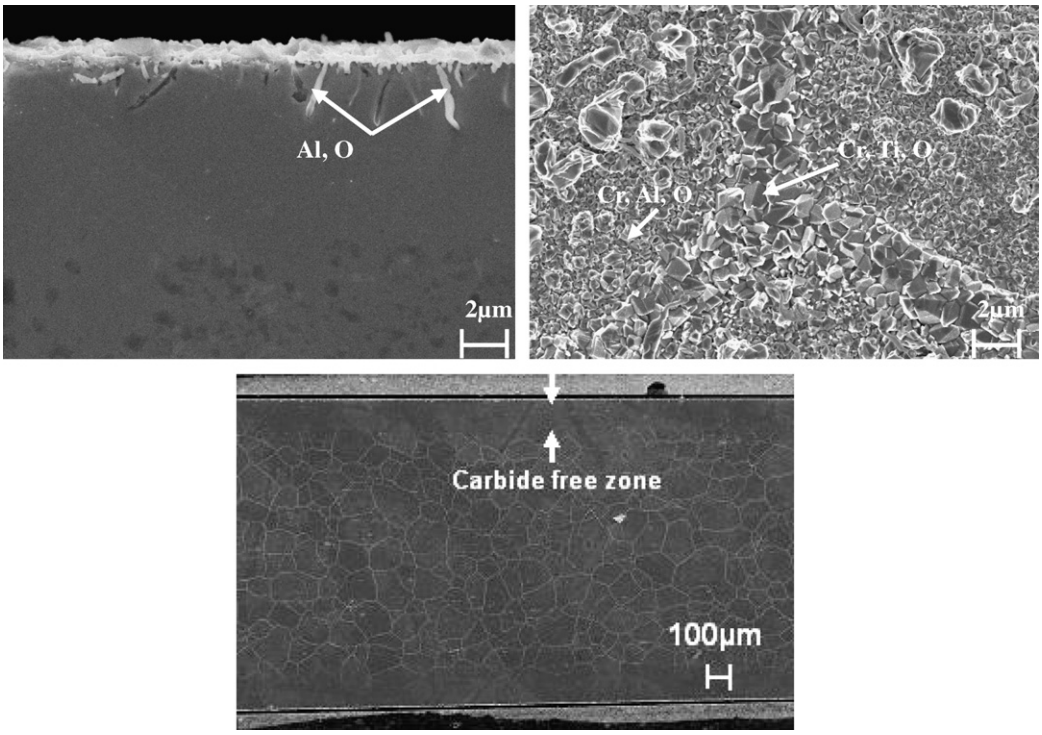

Fig. 4. FESEM images with a secondary electron contrast – cross section and top view of the Alloy 617 surface after step 2 in He–In3.

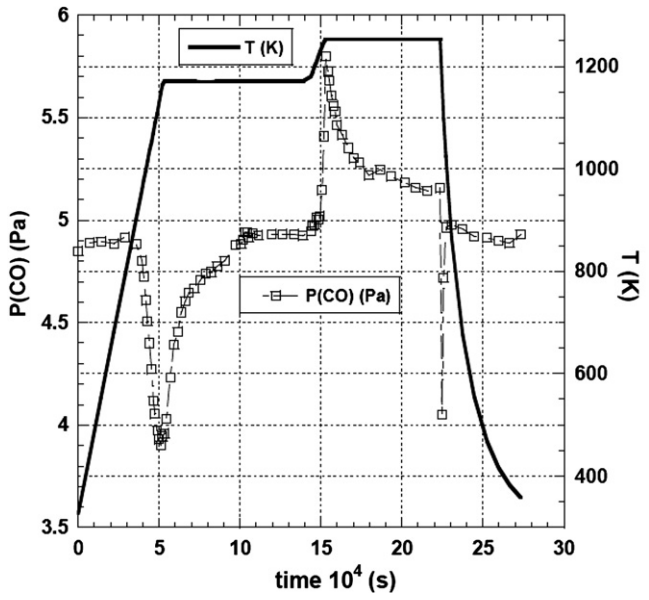

Fig. 5. Temperature program and outlet partial pressure of CO as a function of time – reactivity of Alloy 230 in He–H3.

Table 4
Mean mass change (2 specimens) and approximate thickness of the surface scale (optically evaluated on SEM images) – Alloy 230 specimens after step 1 and after step 2 in He–H3

	Δm (mg/cm^2)	δ_{ox} (μm)
After step 1	$+0.11 \pm 0.01$	~0.7
After step 2	$+0.05 \pm 0.01$	~0.3

and GDOES analyses (see Fig. 8) indicated that the Cr, Mn-spinel is in the upper part of the scale whereas the inner part mainly consists of Cr_2O_3.

The GDOES analysis also identified aluminum and silicon at the scale/alloy interface. EDX showed that a discontinuous aluminum-rich oxide developed underneath the chromium-rich layer and that some aluminum oxidized along the grain boundaries up to 10 μm deep inside the alloy.

4.2.4. Observations and analyses of the Alloy 230 surface after step 2 (above T_A)

Fig. 6, right-hand side, shows the surface of a specimen of Alloy 230 exposed for 20 h at 1253 K in He–H3. A continuous surface oxide film can still be observed. However, this layer is significantly thinner than after step 1 (see Fig. 6, left-hand side, and Table 4). Linescans through the scale by microprobe (WDS) and by GDOES (see Fig. 8) proved that the amount of chromium in the surface oxide decreases when compared to the oxide developed after step 1. On the other hand, the chromium content in the metallic phase under the scale may slightly increase. Manganese and aluminum are detected in the oxide layer after step 2.

4.3. Influence of $P(CO)$ on the critical temperature T_A

Table 2 reports the critical temperature T_A for Alloys 617 and 230 in various impure helium atmospheres. These values were obtained following specific procedures at AREVA NP and at the CEA as explained in Section 3. Fig. 9 plots the measured T_A against P(CO): the higher

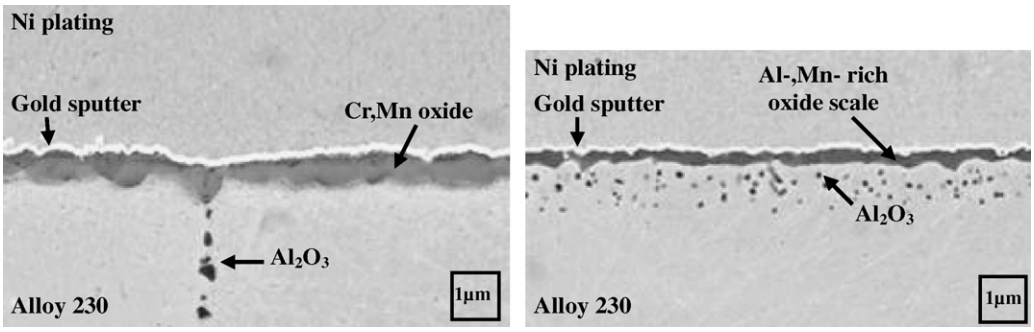

Fig. 6. FESEM images with a backscattered electron contrast at 20 kV – cross-section of the Alloy 230 surface after step 1 (left-hand side) and after step 2 (right-hand side) in He–H3.

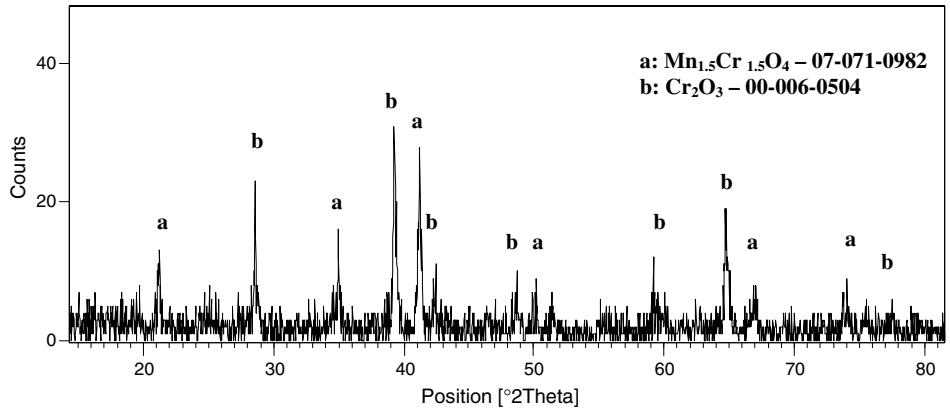

Fig. 7. Grazing XRD analysis at 1° – Alloy 230 surface after step 1.

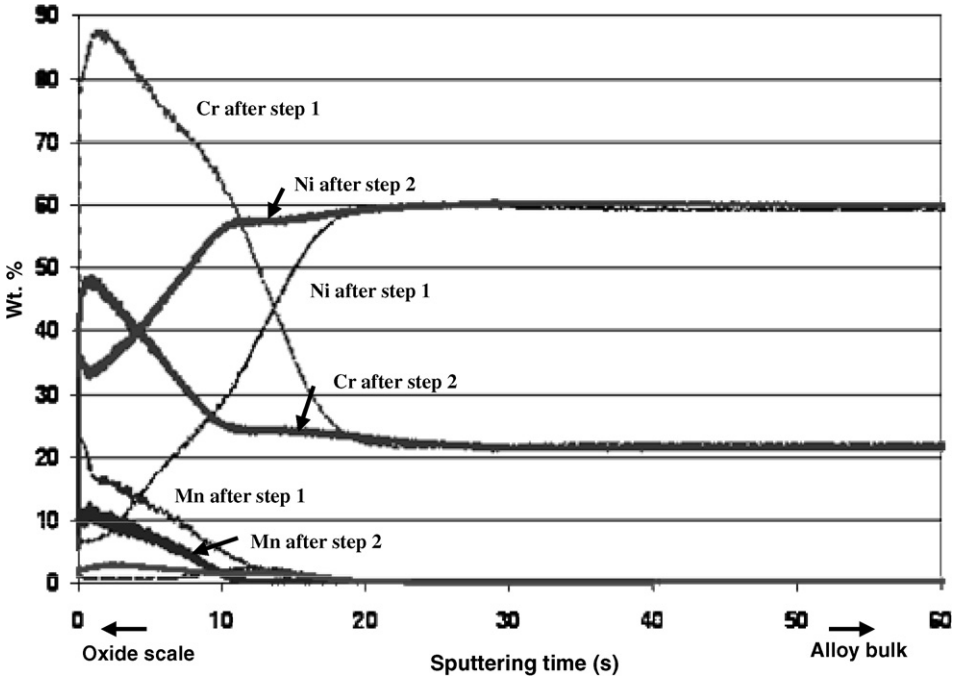

Fig. 8. Profiles of Ni, Cr, Mn by GDOES (oxide scale is on the left-hand side, alloy bulk on the right-hand side) – surface of the Alloy 230 after step 1 and step 2 in He–H3.

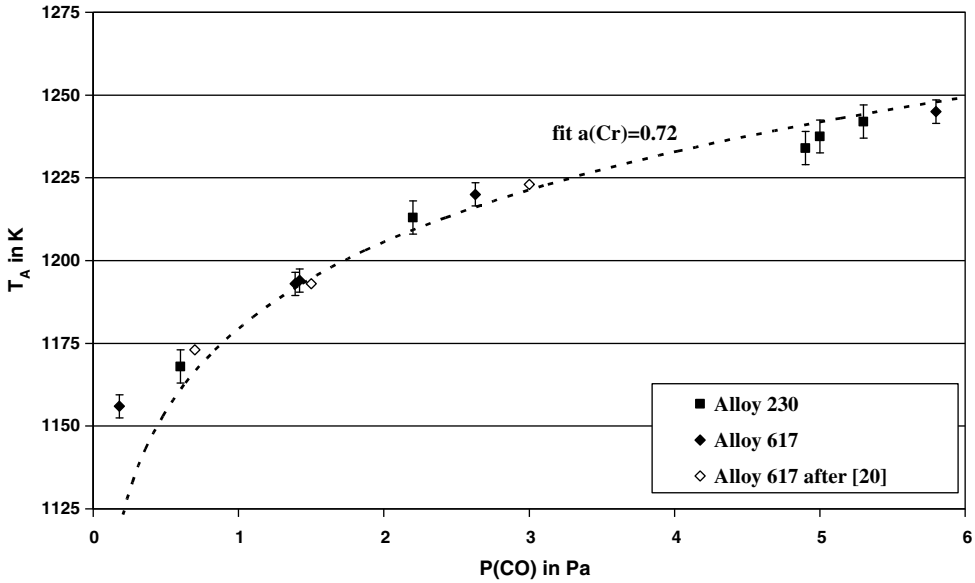

Fig. 9. Critical temperature T_A in impure helium with different P(CO) (see Table 2: He–In1 to He–In6 for Alloy 617 and He–H1 to He–H5 for Alloy 230); published data for Alloy 617 from Ref. [20] in helium-containing 50 Pa H_2, 2.2 Pa CH_4 and ~0.05 Pa H_2O; calculated curve for equilibrium conditions of Eqs. (5) and (9) with a(Cr) = 0.72.

the level of carbon monoxide in the gas phase, the higher T_A. Besides considering the experimental accuracy, both materials present similar dependence for T_A vs. P(CO).

5. Discussion

5.1. Oxidation in impure helium

Both alloys oxidized in the test atmospheres at 1123 K and 1173 K (see Figs. 2 and 6 left-hand side). Two oxidizing gasses can react with the metallic surface: H_2O and CO following, respectively Eqs. (1) and (4). It is worth noticing that reaction of CO after Eq. (4) should deposit some carbon at the reaction site. Figs. 1 and 5 show that some carbon monoxide was consumed during heating of the specimens but this consumption stopped when the temperature was kept constant at $T < T_A$. It is thus assumed that carbon monoxide initially takes part in the oxidation but after a while only water vapor reacts.

A continuous chromium-rich surface oxide formed on both nickel base alloys that contain about 22 wt% Cr. However, minor elements influenced the scale composition. For Alloy 617 (0.4 wt% Ti), titanium was detected in the oxide layer preferentially above the alloy grain boundaries (see Fig. 2). Manganese (0.5 wt% Mn in Alloy 230) dissolved in chromia and was shown to be uniformly spread over the Alloy 230 surface, irrespective of the alloy grains or grain boundary regions (see Fig. 6, left hand side). Manganese that diffuses through Cr_2O_3 about 100 times faster than chromium itself [24] concentrated in the outer zone of the scale as a Mn, Cr-spinel.

Aluminum, which can be oxidized at very low oxygen activities and slowly diffuses within the alloy, internally oxidized mainly at grain boundaries.

5.2. Oxide scale reduction

Gas phase analysis evidenced an increase in the partial pressure of carbon monoxide during heating of specimens in step 2 (starting at about 1194 K for Alloy 617 in Fig. 1). As already discussed in the literature [10,11,14], the whole production of carbon monoxide cannot be explained by a reaction involving water vapor or methane for instance Eqs. (3), (7) or Eq. (8) because the total amount of water vapor in the gas was limited (for instance 0.16 Pa H_2O in He–H3 for a peak CO production of 0.9 Pa in Fig. 5) and CO was produced in CH_4-free atmospheres (see Fig. 1). Another reaction should thus account for the production of CO.

$$H_2O_{(g)} + CH_{4(g)} = CO_{(g)} + 3H_{2(g)} \quad (7)$$

$$Cr_2O_{3(s)} + 3CH_{4_{(g)}} = 2Cr_{(s)} + 3CO_{(g)} + 6H_{2(g)} \quad (8)$$

In the mean time during step 2, specimens lost mass while the thickness of the surface layer decreased as shown in Table 4. This strongly suggests that the surface oxide was reduced following Eq. (6). Considering thermodynamics, chromia and possibly manganese and titanium oxides are ready to be reduced by carbon in the given temperature range. Aluminum oxide can not react in such conditions.

GDOES examinations of Alloy 230 specimens after step 1 and after step 2 (see Fig. 8) indicated that during step 2 the surface oxide was depleted in chromium while the chromium content in the underlying alloy possibly increased. We conclude that the carbon preferentially reduced the chromium oxide rather than the manganese oxide. The specimens of Alloy 230 were further analyzed by GDOES following a specific calibration routine on metallic standards that allowed to quantify carbon profiles with a good

accuracy [3]. It confirmed that the reduction of the oxide layer went together with a depletion of carbon beneath the scale. $C_{(s)}$ likely diffused from the bulk to the scale/alloy interface to react according to Eq. (6).

When the temperature was kept constant at $T > T_A$, Eq. (6) proceeded and could be coupled to other reactions. The surface scale on Alloy 617 was thinner at the beginning of step 2 (see Fig. 3) than at the end of step 2 (see Fig. 4), implying that the specimen further oxidized over step 2. The helium He–In3 was rather rich in water vapor and did not contain any methane. Therefore, the ratio $P(CH_4)/P(H_2O)$ was virtually zero. After Brenner [10,11] (see Section 2.4), we propose that the surface oxide was actually reduced by the carbon in solution following Eq. (6) but it was reformed by reaction with water vapor according to Eq. (1). Carbon, continuously removed from the surface by Eq. (6), thus diffused to the scale/alloy interface. As the carbon activity decreased in the subsurface zone, internal carbides were destabilized according to Eq. (5). That is probably why no carbides are observed under the surface of Alloy 617 up to approximately 120 μm deep in Fig. 4. On the other hand, it was elsewhere shown [2] that, in helium similar to test gas He–H3, Alloy 230 carburized. So, the ratio $P(CH_4)/P(H_2O)$ in He–H3 was high enough for methane to decompose on the surface according to Eq. (2). The carbon deposit by Eq. (2) caused a transport of carbon inside the alloy bulk where coarse metallic carbides precipitated.

In summary, Eq. (6) consumes the surface chromium-rich oxide and the carbon from the alloy. It produces gaseous carbon monoxide and likely metallic chromium. Consequently it may be written as followed:

$$Cr_2O_3 + 3C_{(s)} \overset{T>T_A}{\rightarrow} 3CO + 2Cr \tag{9}$$

Figs. 1 and 5 show that the partial pressure of carbon monoxide at the test section outlet sharply increased at the beginning of step 2. However when the temperature was kept constant at 1253 K, the quantity of CO decreased and the curves $P(CO)$ vs. time exhibited peak shapes. As the reaction rate is proportional to the production of CO, the decrease of $P(CO)$ suggests that the interfacial reaction did not establish the rate but that another slow process limited the rate of Eq. (9). Considering the parabolic shape of the peaks, we can reasonably assume that the rate limiting step was the transport of some reactant or product to/away from the reaction site, such as for instance the diffusion of carbon to the surface.

5.3. Influence of gas composition on the critical temperature T_A

With the assumption that T_A is the equilibrium temperature of Eq. (9), Quadakkers [20] wrote

$$K_9(T_A) = \frac{\left(\frac{P(CO)}{P_{total}}\right)^3 . a(Cr)^2}{a(C_{(s)})^3} \tag{10}$$

with K_9 the equilibrium constant of Eq. (9) and the chromium oxide activity taken as unity.

Quadakkers also stated that Eq. (5) reaches equilibrium. So, the carbon activity in the alloy is determined by

$$a(C_{(s)}) = \frac{K_5(T_A)^{\frac{1}{6}}}{a(Cr)^{\frac{23}{6}}} \tag{11}$$

with K_5 the equilibrium constant of Eq. (5) and the carbide activity taken as unity.

Eqs. (10) and (11) can be combined to calculate a theoretical relation that links T_A and $P(CO)$, the chromium activity at the scale/alloy interface being the only unknown factor. By using the thermodynamic data from the HSC software [25] for K_5 and K_9, Fig. 9 proposes the best fit for the results on Alloys 617 and 230. It corresponds to an interfacial chromium activity of 0.72. As already noticed by Quadakkers [20], the theoretical curve presents an appropriate shape but the value of $a(Cr)$ is problematic. Although the chromium activity in Alloy 230 is unknown, activity data were published for Alloy 617. The bulk $a(Cr)$ reaches about 0.35 in Alloy 617 in the temperature range 1173–1223 K [20]. The large discrepancy between extrapolated and effective chromium activity in Alloy 617 emphasizes that this basic thermodynamic approach can not properly model the reduction of the surface oxide. Hence we presume that either Eqs. (10) and (11) are essentially irrelevant, or that some considered reactant and/or product is inappropriate or that some thermodynamic data are inaccurate for the given system.

5.4. Influence of the alloy composition on the critical temperature T_A

Both alloys exhibited a similar dependence of T_A vs $P(CO)$ in impure helium as shown in Fig. 9. For Alloy 230, chromium was shown to be the more reactive element regarding Eq. (6) and we can reasonably assume that Alloy 617 also experienced a preferential reduction of the chromium-rich oxide. Identical curves T_A vs. $P(CO)$ for the two materials should correspond to identical equilibrium conditions of Eq. (9) although we would expect differences in the activities of $C_{(s)}$ and chromium.

6. Conclusion

The ANTARES project addresses, among others, the crucial issue of selecting a material for the IHX of an advanced VHTR. Operation in impure helium at temperatures as high as 1223 K creates very demanding requirements for the thin IHX structural metallic plates in terms of thermal stability, creep strength, and environmental compatibility with the primary coolant. Feedback from the former helium-cooled reactors emphasized that helium impurities react toward chromium-containing nickel base alloys, especially Alloy 617. These surface interactions

can cause in-depth changes in the microstructure that irreversibly alter the mechanical properties. Accordingly, long service lifetime relies on the growth of a protective surface scale which basically must suppress or strongly slowdown exchanges between the atmosphere and the metallic surface. It was shown that Alloy 617 is ready to develop a chromia layer in 'balanced' helium, meaning with a moderate carbon potential and oxidizing toward chromium. However, this surface scale can suffer from a destructive process at high temperatures and cannot protect against corrosion.

Following a procedure adapted from Quadakkers [20], AREVA NP validated the reactivity of the Alloy 617 surface in impure helium. The CEA also tested Alloy 230, an alternative IHX candidate material, which corrosion behavior has never been investigated in VHTR environment so far. In the given conditions, interactions of helium impurities toward both alloys result either in the oxide scale formation at temperatures below T_A or in the oxide reduction above T_A.

Below the critical temperature T_A, Alloy 617 develops a chromium-rich oxide scale, locally doped with titanium. A mixed manganese and chromium oxide grows on the Alloy 230 surface. The two alloys suffer from internal oxidation of aluminum.

Above T_A, the oxide layer is partly reduced with a concurrent production of carbon monoxide. For Alloy 230 [2,3], it has been established that:

- the surface oxide is reduced by the carbon from the alloy,
- the chromium-rich oxide preferentially reacts,
- together with carbon monoxide, the reaction produces metallic chromium that may diffuse away from the oxide/alloy interface.

Finally the global process for Alloy 230, and possibly also for Alloy 617, can be summarized by Eq. (9). The critical temperature T_A significantly depends on the carbon monoxide partial pressure in helium. A simple thermodynamic treatment based on the equilibrium conditions for Eqs. (5) and (9), allows to qualitatively explain the effect of $P(CO)$ on T_A. However, the proper fit of the experimental data considers a surprisingly high local chromium activity. To go further with the thermodynamic modeling, surface activities of chromium and internal carbon need to be accurately measured or calculated.

Unexpectedly, the two nickel base alloys exhibit almost the same dependence of T_A vs. $P(CO)$.

Above T_A, Eq. (9) the chromium-rich protective surface oxide is reduced according to Eq. (9) whatever the environmental conditions. It is worth noticing that the scale reduction can be very fast. Within 20 h at 1253 K, more than half of the oxide layer on Alloy 230 has been reduced in helium He–H3. Eq. (9) thus jeopardizes the material resistance and its critical temperature T_A imposes an ultimate operating point for a VHTR. However as already mentioned, T_A is strongly related to the gas phase composition – for Alloy 617, T_A goes from about 1156 K to 1245 K when the partial pressure of carbon monoxide changes from 0.18 Pa to 5.8 Pa. In other words for a given service temperature (including safety margins), Fig. 9 gives the minimum allowable $P(CO)$ in the coolant helium.

From the operational viewpoint, major implications are:

- the analytical systems must assess the gas phase composition, especially the CO content, with a good accuracy in the whole primary circuit,
- the chemical purification unit must warrant that the carbon monoxide content continuously remains in a given range, or at least above a minimum value, at any moment, in any part of the circuit.

Acknowledgements

The authors wish to thank Mr P. Bonnaillie of CEA/DEN/DANS/DMN/SRMP for the valuable FESEM observations and analyses, Ms M.C. Lafont of the Université Paul Sabatier, Toulouse for the TEM analyses and Mr M. Tabarant of CEA/DEN/DANS/DPC/SCP for the GDOES analyses.

References

[1] J.-C. Gauthier, G. Brinkman, B. Copsey, M. Lecomte, Nucl. Eng. Des. 236 (2006) 526.
[2] F. Rouillard, C. Cabet, A. Terlain, K. Wolski, in: Proceedings of Eurocorr 2005, Libon, Portugal, 2005, Paper O-358-8.
[3] F. Rouillard, C. Cabet, K. Wolski, A. Terlain, M. Tabarant, M. Pijolat, F. Valdivieso, J. Nucl. Mater. 362 (2007) 248.
[4] J. Chapovaloff, D. Kaczorowski, K. Wolski, in: Proceedings of Matériaux 2006, Dijon, France, 2006.
[5] J. Chapovaloff, D. Kaczorowski, G. Girardin, A. Pages, in: Proceedings of EFC-Event No. 290, Frankfurt am, Germany, 2006.
[6] L.W. Graham, M.R. Everett, D. Lupton, F. Ridealgh, D.W. Sturge, M. Wagner-Löffler, in: Proceedings of the Jülich symposium on Gas-cooled reactors with emphasis on advanced systems, vol. I, IAEA Eds., Vienna, Paper No. IAEA-SM200/82, 1976, p. 319.
[7] R. NiederProceedings of the Gas-Cooled Reactors Today, vol. 2, BNES Eds., London, 1982, p. 91.
[8] K. Krompholz, J. Ebberink, G. MenkenProceedings of the 8th International Congress on Metallic Corrosion, vol. II, Dechema Eds., Frankfurt, 1981, p. 1613.
[9] G.E. Wasielewski, A.M. Beltran, H.M. Fox, F.E. Sczerzenie, in: Proceedings of the Jülich Symposium on Gas-cooled Reactors with Emphasis on Advanced Systems, vol. I, IAEA Eds., Vienna, Paper No. IAEA-SM200/56, 1976, p. 379.
[10] K.G.E. BrennerProceedings of the Gas-Cooled Reactors Today, vol. 2, BNES Eds., London, 1982, p. 191.
[11] K.G.E. Brenner, L.W. Graham, Nucl. Technol. 66 (1984) 404.
[12] G. Menken, R. Nieder, W.L. Graham, W. ThieleProceedings of the Gas-Cooled Reactors Today, vol. 2, BNES Eds., London, 1982, p. 185.
[13] M.R. Warren, High Temp. Technol. 4 (1986) 119.
[14] W.J. Quadakkers, H. Schuster, Werkst. Korros. 36 (1985) 141.
[15] P.J. Ennis, D.F. Lupton, The Relationship Between Carburisation and Ductility Loss, The Metals Society Eds., London, 1980, p. 979.
[16] H.E. McCoy, J.P. Strizak, J.F. King, Nucl. Technol. 66 (1984) 161.

[17] R.H. Cook, Nucl. Technol. 66 (1984) 283.
[18] T. Nakanishi, H. Kawakami, Nucl. Technol. 66 (1980) 273.
[19] Y. Kurata, Y. Ogawa, H. Nakajima, T. Kondo, in: Proceedings of the Workshop on Structural Design Criteria for HTR, Jülich, Germany, 1989, p. 275.
[20] W.J. Quadakkers, Werkst. Korros. 36 (1985) 335.
[21] H.J. Christ, U. Künecke, K. Meyer, H.G. Sockel, Mater. Sci. Eng. 87 (1987) 161.
[22] Y. Maru, Y. Kuramasu, Y. Awakura, Y. Kondo, Metall. Trans. 4 (1973) 2591.
[23] C. Cabet, A. Terlain, G. Girardin, D. Kaczorowski, M. Blat, J.L. Séran, S. Dubiez Le Goff, in: Proceedings of ICAPP 2007, Nice, France, 2007, Paper 7192.
[24] D.F. Lupton, Mechanisms of Surface Scale formation in HTR helium, Report No. JÜL-1639, Kernforschungsanlage Jülich GmbH, 1980.
[25] HSC Chemistry 5.11, Outokompu Research Oy, Pori, Finland, 2002; data for Cr_2O_3 after I. Barin, Thermochemical Data of the Pure Substance, 1989; data for $Cr_{23}C_6$ after I. Barin, Thermochemical Data of the Pure Substance Part II, 1993.